

Article

Catalytic Hydrogenation, Hydrodeoxygenation, and Hydrocracking Processes of a Lignin Monomer Model Compound Eugenol over Magnetic Ru/C–Fe₂O₃ and Mechanistic Reaction Microkinetics

Ana Bjelić^{1,2}, Miha Grilc^{1,*} , Sašo Gyergyek³, Andraž Kocjan⁴ , Darko Makovec³ 
and Blaž Likozar¹

¹ Department of Catalysis and Chemical Reaction Engineering, National Institute of Chemistry, Hajdrihova 19, 1001 Ljubljana, Slovenia; ana.bjelic@ki.si (A.B.); blaz.likozar@ki.si (B.L.)

² Faculty of Chemistry and Chemical Technology, University Ljubljana, Večna pot 113, 1001 Ljubljana, Slovenia

³ Department of Synthesis of Materials, Jožef Stefan Institute, Jamova Cesta 39, 1001 Ljubljana, Slovenia; saso.gyergyek@ijs.si (S.G.); darko.makovec@ijs.si (D.M.)

⁴ Department of Nanostructured Materials, Jožef Stefan Institute, Jamova Cesta 39, 1001 Ljubljana, Slovenia; andraz.kocjan@ijs.si

* Correspondence: miha.grilc@ki.si; Tel.: +386-1-4760-283

Received: 13 September 2018; Accepted: 25 September 2018; Published: 28 September 2018



Abstract: Conversion of waste lignocellulosic (LC) biomass, a widely-available low-cost feedstock, into value-added biobased chemicals (and biofuels) has been gaining much attention recently. Therefore, the present lignin valorisation study was aimed at developing magnetically-separable highly-active catalysts for hydrodeoxygenation (HDO), also proposing surface chemical kinetics. Five carbonaceous substrate-deposited Ru were synthesised and tested for the HDO of monomer moiety eugenol. Their annealing temperatures differed, specifically between 300 and 750 °C, while one was not subjected to calcination. Experiments revealed the substantial influence of annealing temperature on the product distribution. Namely, fresh nonannealed nanocomposites were not active for hydrogenolysis. By further pretreatment increase, hydrogenation and, exclusively, the deoxygenation of saturated cyclic species, were enhanced, these being more promoted considering rates and yields than commercial carbon-supported ruthenium. Over 80 mol% of 4-propyl-cyclohexanol and propyl-cyclohexane could be formed over the samples, treated at 500 and 600 °C, for 100 and 125 min, respectively, under 275 °C and 5 MPa of reactor hydrogen pressure. Interestingly, a notable 4-propyl-phenol amount was produced upon 750 °C pretreating. The intrinsic microkinetic model, developed previously, was applied to determine relevant turnover parameters. Calculated modelling results indicated a 47- and 10-fold greater demethoxylation and dehydroxylation mechanism ability upon the reheating/preheating at 600 °C in comparison to industrial (heterogeneous) Ru/C.

Keywords: biomass-derived chemicals; recyclable ruthenium catalyst; heteroatom removal; hydroprocessing; structure–activity relationship; intrinsic kinetics modelling

1. Introduction

Lignocellulosic (LC) biomass is available in the form of agricultural residues, waste streams (pulp, paper, and food industry), wood, and energy crops. It is consisted of cellulose (40–50%), hemicellulose (15–30%), and lignin (15–30%) [1]. Lignin is a complex heteropolymer which plays several important

roles in plants like mechanical support to the sap-conducting xylem cells, plant defence against parasitic and enzymatic attacks, seed dispersal, and the formation of an apoplastic diffusion barrier in the roots [2,3]. Its monolignol units are interconnected via different ethers and carbon-carbon bonds (β -O-4, α -O-4, biphenyl, β -5) forming a randomised network by a radical polymerisation in the cell wall [4]. Lignin is a feedstock rich in aromatic functionality and represents a significant portion of the total carbon in biomass [5]. Hence, valorisation of this abundant feedstock is required for improving the economic balance of any biorefinery [1]. Beside lignin's transformation into chemicals (i.e., benzenes, cycloalkanes, phenols, and styrene) comprehensively reviewed by Isikgor and Becer [6], it can also be converted into carbonaceous fibre nanocomposites, and other added value products [7-9]. For instance, Agblevor and Jahromi reported an aqueous phase hydrotreatment of guaiacol forming significant amounts of benzene, toluene, and cyclohexane and minor formation of xylene, phenol, catechol, and anisole over a novel catalyst based on the nickel-impregnated red mud in a one-pot process [10]. The product distribution was similar also at nonaqueous experimental conditions [11].

Over years many catalysts based on transition (Ni, Mo, Cu, Co, and Fe) and noble metals (Pt, Pd, Rh, and Ru) have been tested for LC biomass valorisation. Heterogeneous catalysis simplifies the separation of the liquid products from the solid catalyst and its recycling. However, the separation by filtration or centrifugation can be often difficult, especially when the catalyst is in powder form. The use of magnetically separable catalysts helps to overcome these obstacles since they can be easily and efficiently removed from reaction mixtures by applying an external magnetic field gradient [12]. Liu et al. [13] have synthesised magnetic nitrogen-doped carbon-supported cobalt nitride ($\text{CoN}_x@\text{NC}$) and tested it for HDO of eugenol. They demonstrated different activity and selectivity of catalysts pyrolysed at various temperatures (500-800 °C). More literature is available for conversion of cellulose derivatives over magnetic catalysts such as sulphonated mesoporous silica ($\text{Fe}_3\text{O}_4\text{-SBA-SO}_3\text{H}$), Co-based sulphonated silica ($\text{CoFe}_2\text{O}_4@\text{SiO}_2\text{-SO}_3\text{H}$), core-shell structured $\text{Fe}_3\text{O}_4@\text{C-SO}_3\text{H}$, and magnetic biocatalysts (enzymes immobilised on a magnetic support) [13]. Magnetically separable carbon supports can be prepared by impregnation of carbon material with magnetic nanoparticles, or to form carbon material in the presence of magnetic nanoparticles and thus incorporating them within the carbon support. The carbon support is usually prepared by pyrolysis of organic precursors, e.g., carbohydrates at 450 to 1500 °C [14]. In this work the magnetically separable carbon support was prepared by hydrothermal treatment of glucose in the presence of magnetic nanoparticles followed by annealing in an inert atmosphere. Ru nanoparticles were deposited on the surface of the support in a subsequent step. This work emphasized on the influence of annealing at four different temperatures (none, 300, 500, 600, and 750 °C) on catalytic hydrotreatment activity for lignin-derived monomer compound eugenol. The aim of this work is to quantitatively determine the structure-activity correlation based on the thorough catalyst characterization and kinetic parameters determined by the microkinetic model, presented in our previous work [15]. Synthesised catalysts have not been tested in a mixture of several model compounds or actual lignin bio-oil at this level of the research; although it is expected to be implemented in the future work. It is of course important that catalysts retain activity and selectivity, not only in contact with a single reactive molecule, but also in a mixture of model compounds (simulating lignin derived bio-oil mixture) or for the actual lignin-derived bio-oil. However, eugenol has been chosen as a model compound as it contains hydroxy, methoxy, and allyl functional groups on an aromatic ring that are all also present in lignin monomers. Hence the HDO of eugenol yields several products which can be formed during the lignin depolymerisation and further upgrading of building blocks and are also representative from the group-complexity point of view. Additionally, the focus of the present study is primarily a kinetic study, which might be difficult in the case of complex feedstock and corresponding reaction mechanism. This can result in misconclusions and related irrelevance of the determined kinetic parameters. For that reason, the presents study only provides a starting point for further investigation on a real lignin-derived bio-oil. Agblevor and Jahromi, for example, have not observed a significant

difference in reactivity when the hydrotreatment of model compounds or real biomass pyrolysis oil was investigated [16].

2. Model

A detailed model development has been presented in our previous study [15], therefore only a brief model presentation is provided in Supplementary Information. The model is aimed to describe the complex behaviour of a three-phase slurry reactor without predetermination of the rate limiting steps by taking into account phenomena such as hydrogen dissolution in the liquid phase, transport through the films around bubbles and catalyst particles, reactions in the liquid phase, adsorption and desorption of the components, and chemical transformations of adsorbed species. The reactor geometry, process conditions (actual temperatures and pressures, mass of the catalyst, initial reactant concentration, stirring rate, and reaction time), and the catalyst's characteristics (e.g., concentration of active sites and specific surface area) are also involved in the model formulation. Absence of the mass transfer limitations has been assured by intensive mixing, as it has been quantitatively shown in the previous study [15]. Heat transfer effects are likely to be absent considering several aspects commented in detail in our previous work [15]. Specifically, according to the Prater criterion (lower than 1), absence of temperature gradient within the catalyst particles was confirmed.

3. Results and Discussion

3.1. Catalyst Characterization

Each catalyst is composed of three distinctively different phases of magnetic nanoparticles (first phase) incorporated within the carbonaceous matrix (second phase) representing together a magnetically separable support for Ru nanoparticles (third phase). X-Ray Diffraction (XRD) patterns (Figure 1) of Ru/C-Fe₂O₃, Ru/C-Fe₂O₃-300, and Ru/C-Fe₂O₃-500 are composed only of reflections characteristic of magnetic iron oxide and a broad hump at low angles characteristic of amorphous material. Average crystallite size of the iron oxide nanoparticles was found to be approx. 14 nm. XRD pattern of the Ru/C-Fe₂O₃-600 shows an additional weak reflection, a characteristic of nonmagnetic iron oxide FeO and BCC Fe indicating partial reduction of iron oxide. The composition of the Ru/C-Fe₂O₃-750 is significantly different. The catalyst is composed of cohenite Fe₃C and nanocrystalline graphite as main phases and smaller amounts of BCC Fe and magnetic iron oxide. Reflections characteristic of Ru were not observed in any of the XRD patterns suggesting its amorphous state. We can conclude that until 500 °C was reached the iron oxide nanoparticles remain practically intact. At 600 °C, a slow reduction occurs, and at 750 °C, most of the iron oxide reduces to Fe which substantially transforms to Fe₃C. Reduction is most likely due to CO that forms during decomposition of carbonaceous matter. More detailed characterisation results for the Ru/C-Fe₂O₃-750 are available in our previous work [17].

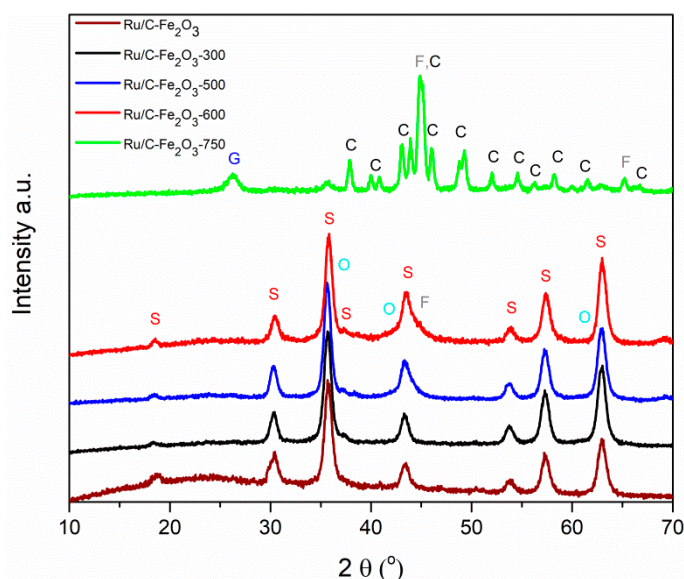


Figure 1. XRD patterns of catalysts. S corresponds to reflections of cubic spinel-iron oxide, F of BCC iron, O of wustite, C of cohenite, and G of graphite.

Transmission Electron Microscopy (TEM) imaging of the catalyst particles revealed large differences between them in many aspects, such as distribution of magnetic phases within the carbonaceous matrix, size, and dispersion of the Ru nanoparticles for example (Figure 2). Iron-oxide nanoparticles are visible as dark approximately spherical particles incorporated within the grey matrix of uniform and low contrast (Figure 2a,b). Ru nanoparticles are visible as smaller dark particles seen mostly at higher magnification (Figure 2d,f,h,j). Particles of the catalyst Ru/C-Fe₂O₃ appear as branched and rounded. Ru nanoparticles are barely visible and their number is relatively low in agreement with observed incomplete reduction of Ru³⁺. Particles of catalyst Ru/C-Fe₂O₃-300 appear more compact and covered with Ru nanoparticles that are predominantly clustered and of relatively broad size distribution (Figure 2c,d and Figure 3, Table 1). It should be mentioned that, also, in this case, the reduction of Ru³⁺ was incomplete; however, it proceeded much further than in the case of Ru/C-Fe₂O₃. Particles of Ru/C-Fe₂O₃-500 are even more compact and completely covered with Ru nanoparticles of largest average size (Figure 2e,f and Figure 3, Table 1). Particles of catalyst Ru/C-Fe₂O₃-600 appear similar but less densely covered with Ru nanoparticles (Figure 2g,h). Ru nanoparticles are of two different sizes; smaller spherical and larger plate-like (Figure 2h). In Table 1 and Figure 3 only the size distribution of smaller spherical ones is presented. Larger plate-like nanoparticles are predominantly oriented with the basal plane parallel to the electron beam making estimation of their size unreliable. However, a rough estimation of their thickness is 3 nm and the diameter of basal plane is 15 nm. TEM analysis of the catalyst Ru/C-Fe₂O₃-750 reveals rather irregular shape of particles (Figure 2i). Larger Fe and Fe₃C nanoparticles of dark contrast are clearly visible within the matrix. Observation at higher magnification revealed that nanoparticles are enclosed with graphitic layer. Ru nanoparticles are homogeneously distributed over the support (Figure 2j).

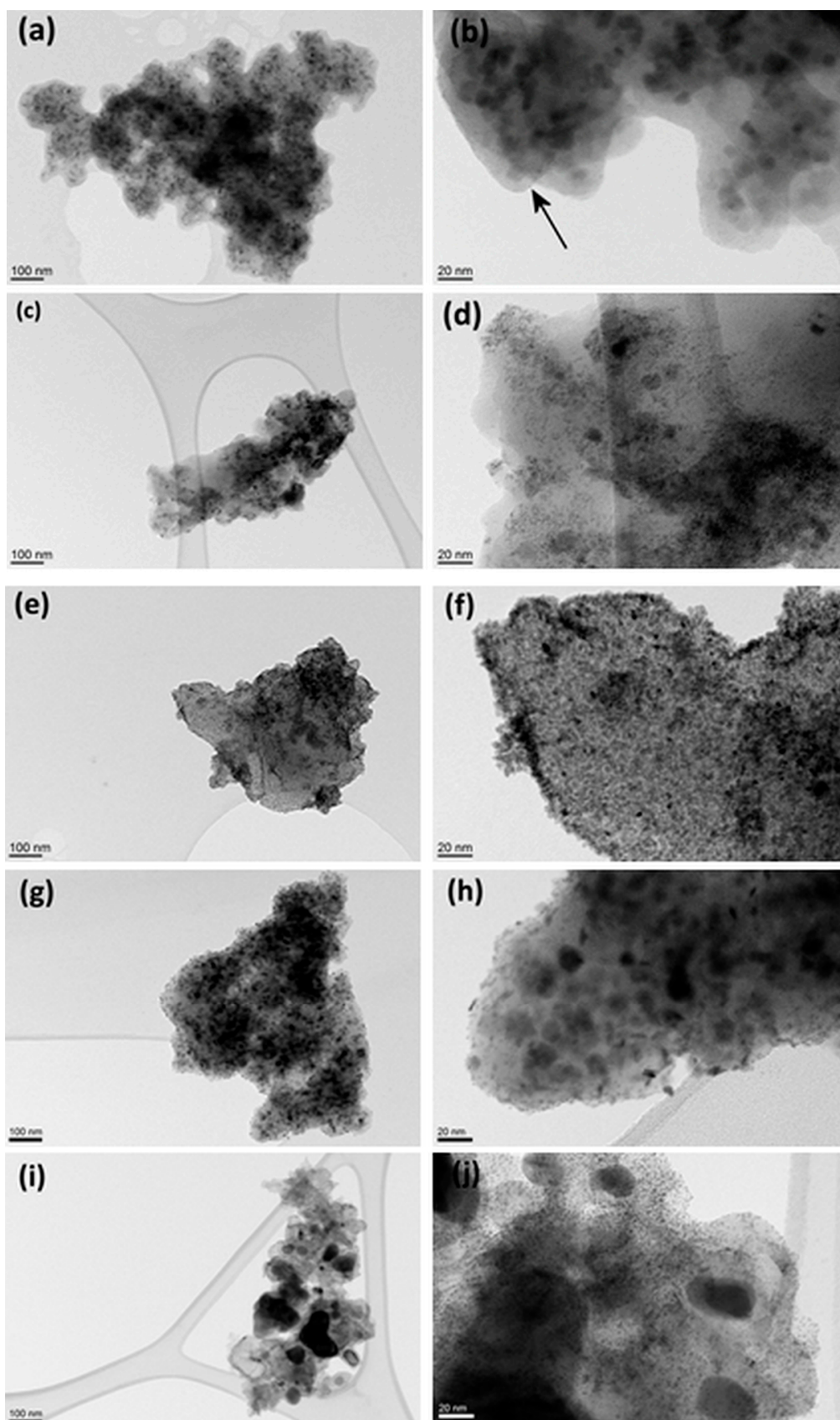


Figure 2. Transmission electron microscopy (TEM) images of catalysts (a,b) Ru/C-Fe₂O₃, (c,d) Ru/C-Fe₂O₃-300, (e,f) Ru/C-Fe₂O₃-500, (g,h) Ru/C-Fe₂O₃-600, and (i,j) Ru/C-Fe₂O₃-750. An Ru nanoparticle is marked with the arrow ion the image (b).

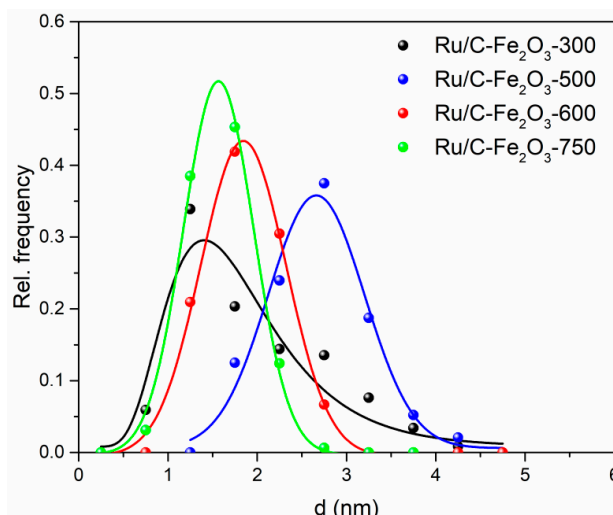


Figure 3. Empirical size distribution of functions of Ru nanoparticles fitted with Gaussians for the catalysts Ru/C-Fe₂O₃, Ru/C-Fe₂O₃-500, Ru/C-Fe₂O₃-600, Ru/C-Fe₂O₃-750, and log-normal distribution function for the catalyst Ru/C-Fe₂O₃-300.

Room-temperature magnetisation curves of the catalysts, except Ru/C-Fe₂O₃-750, exhibited behaviour characteristic of the superparamagnetic state, namely showing zero coercivity and remanence (Figure 4). Catalyst Ru/C-Fe₂O₃-750 exhibited ferromagnetic behaviour characteristic of Fe₃C [18,19]. Saturation magnetisation of the catalyst is proportional to the amount of incorporated magnetic nanoparticles. With increased temperature of annealing of the support the saturation magnetisation increased until 500 °C indicating partial loss of nonmagnetic carbonaceous matter (Figure 4 and Table 1). The drop in saturation magnetisation for the catalyst Ru/C-Fe₂O₃-600 is related to the formation of nonmagnetic FeO during annealing of the support at 600 °C (Figure 1 and Table 1). Substantial increase of saturation magnetisation of the catalyst Ru/C-Fe₂O₃-750 is related to formation of Fe and Fe₃C which both display much higher saturation magnetisations than magnetic iron oxide (Figure 1 and Table 1) [18,19]. Magnetic properties of the catalyst assured their rapid separation from reaction mixture using simple permanent magnet (Figure S1).

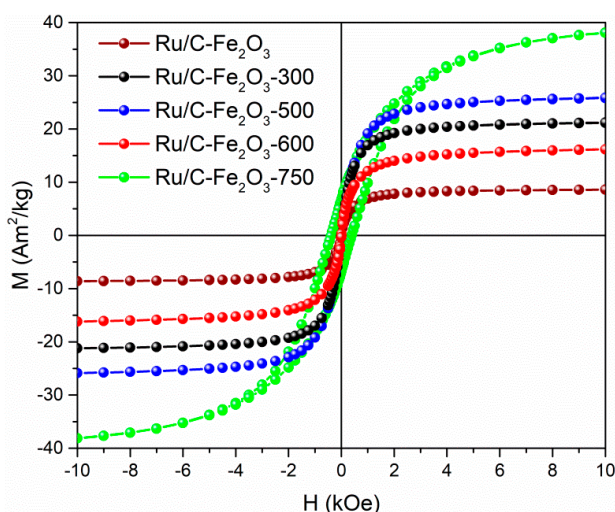


Figure 4. Room-temperature magnetisation curves for the catalysts Ru/C-Fe₂O₃, Ru/C-Fe₂O₃-300, Ru/C-Fe₂O₃-500, Ru/C-Fe₂O₃-600, and Ru/C-Fe₂O₃-750.

The typical nitrogen adsorption–desorption isotherms of all the catalysts employed in the present study are presented in Figure 5. Catalysts Ru/C-Fe₂O₃, Ru/C-Fe₂O₃-300, Ru/C-Fe₂O₃-500,

and Ru/C-Fe₂O₃-600 all exhibit Type I isotherms represented by microporous solids, since they are composed of carbonaceous matrix, and thus having a relatively small external surface. This is also typical for activated carbons and zeolites (where the limiting uptake is governed by the accessible micropore volume rather than internal surface area). The result also corroborates well with the TEM micrographs of catalysts (Figure 2a–h), where there is absence of obvious/substantial meso-to-macroporosity in the catalysts. The Ru/C-Fe₂O₃ catalyst exhibit the shallowest isotherm with the lowest nitrogen uptake, which is directly reflected in the lowest Brunauer-Emmett-Teller (BET) surface area of 8.4 m² g⁻¹ and pore volume of 0.089 cm³ g⁻¹ (Table 1), as a result of low number of barely visible Ru nanoparticles (Figure 2a,b). The catalyst Ru/C-Fe₂O₃-300 exhibits an open-like, low pressure hysteresis, extending to the lowest attainable pressures (Figure 5), which was unchanged even after prolonged equilibration time of the measurement (240 s instead of 60 s). The phenomenon can in principle be related to the swelling of a nonrigid porous structure, with the irreversible uptake of molecules in pores or an irreversible chemical interaction of the adsorbate with the adsorbent [20]. However, considering the chemical properties of the catalyst Ru/Fe₂O₃-300, the first explanation seems most reasonable. The BET surface area and the pore volume of Ru/C-Fe₂O₃-300 in comparison to Ru/C-Fe₂O₃ catalysts were increased to 77 m² g⁻¹ and 0.176 cm³ g⁻¹, respectively (Table 1). The increase can be attributed to the formation of compact clusters of Ru nanoparticles of relatively broad size distribution. By further increase in the annealing temperature of the catalyst preparation to 500 and 600 °C, the microporous network channels were seemingly further evolved as evident from the surface properties (Table 1). Namely, the BET surface area of Ru/C-Fe₂O₃-500 and Ru/C-Fe₂O₃-600 increased to 209 and 259 m² g⁻¹, while the pore volume increased to 0.165 to 0.398 cm³ g⁻¹, respectively. The reason for such increase is twofold. Firstly, it can be associated with the compositional change of the catalysts, with the formation of partly reduced, nonmagnetic iron oxide FeO and BCC Fe phases (Figure 1). Secondly, it can be also ascribed to the pronounced formation of Ru nanoparticles that are, in the case of Ru/C-Fe₂O₃-500, the largest in average size, more compact, and completely covering the catalyst (Figure 2e,f and Figure 3, Table 1), while in the case of Ru/C-Fe₂O₃-600 (Figure 2h), they are of two different sizes, i.e., smaller spherical and larger plate-like (Figure 2h). The Type I isotherm of the catalyst Ru/C-Fe₂O₃-750 annealed at the highest temperatures was the only one to display a typical hysteresis loop at the highest p/p₀ pressures, which is typical for very narrow slit-like pores originating from the aggregates of loosely coherent particles. While on one hand, the formation of well-crystalline cohenite Fe₃C particles (and nanocrystalline graphite) (Figures 1 and 2j) possibly attributed to the lowered BET surface area, i.e., 74 m² g⁻¹ (Table 1), on the other hand, the decomposition of carbonaceous matter forming CO could well be responsible for “loosening” of the catalysts, providing an observed hysteresis loop (Figure 5) and a relatively high pore volume of 0.236 cm³ g⁻¹.

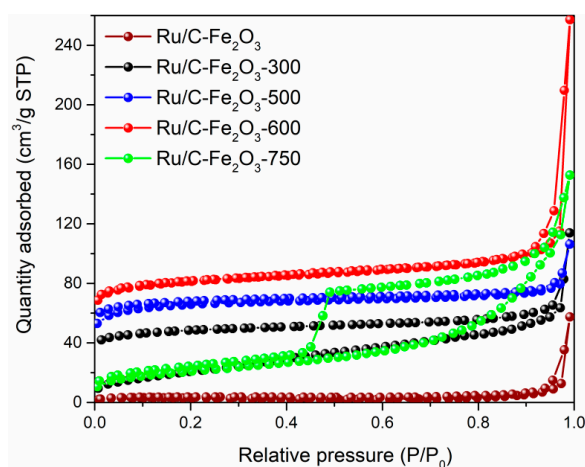


Figure 5. The typical nitrogen adsorption–desorption isotherms of all tested catalysts.

Table 1. Effect of the annealing temperature on properties of catalysts.

Sample	M_s (emu g ⁻¹) ^a	A_{BET} (m ² g ⁻¹)	V_p (cm ³ g ⁻¹) ^b	d_{Ru} (nm) ^c	$CO_{(AS)}$ (mol g ⁻¹)
Ru/C-Fe ₂ O ₃	8.6	8.4	0.089	/	$(7.8 \pm 0.1) \times 10^{-5}$
Ru/C-Fe ₂ O ₃ -300	21.2	77	0.176	1.9 ± 0.8	$(6.13 \pm 0.08) \times 10^{-5}$
Ru/C-Fe ₂ O ₃ -500	25.9	209	0.165	2.7 ± 0.6	$(5.72 \pm 0.03) \times 10^{-5}$
Ru/C-Fe ₂ O ₃ -600	16.2	259	0.398	1.8 ± 0.5 ^d	$(7.77 \pm 0.01) \times 10^{-5}$
Ru/C-Fe ₂ O ₃ -750	38.1	74	0.236	1.5 ± 0.4	$(7.6 \pm 0.4) \times 10^{-5}$

^a Room-temperature magnetisation at $H = 10$ kOe. ^b Pore volume ^c Average diameter of Ru nanoparticles ^d Average diameter of small spherical nanoparticles, larger plate-like were excluded.

CO-TPD profiles are provided in Figure 6, while the amount of metal active sites in Table 1. Densities of active sites available for CO adsorption did not differ much among the catalysts; therefore, very significant differences in catalytic activities might be caused by having fewer active sites available for reactions. It might be worth mentioning that CO-TPD desorption profiles were differing in the number and the shape of peaks among the catalyst as Figure 6 displays. Namely, CO desorption from nonannealed catalyst (wine line) resulted in two observable peaks, one strong at temperatures between 420 and 520 °C and other low and broad between temperatures 520 and 700 °C. This might indicate the presence of both weak and strong active sites, whereas weak are more dominant. Consequently the catalyst might catalyse various reactions with low activity. For the catalyst treated at 300 °C (black line), one broad peak, in the temperature range from 490 to 680 °C, was formed. According to the peak shape, one might say that the peak is composed of one sharp peak at 550 °C and a shoulder at 580 °C. Similar to the first, it could indicate the existence of moderately strong active sites and, therefore, moderate activity for both types of reaction (hydrogenation and deoxygenation). CO desorption from Ru/C-Fe₂O₃-500 (blue line) resulted in one strong and sharp peak in the range of 450 to 600 °C and one shoulder in between 600 and 700 °C. Such a CO-TPD profile could again indicate the presence of two types of active sites; moderately strong and dominant and another even stronger but present in small quantities. For the catalyst annealed at 600 °C (red line), one strong, sharp peak was observed ranging from 420 to 550 °C. Analogously to the previous cases, a single, intensive peak might point to the dominant presence of one type of moderate to strong active site, further indicating higher activity of the catalyst for one or more reactions. The Ru/C-Fe₂O₃-750 showed one broad, intensive peak ranging from 480 to 680 °C (green line). The amount of acid active sites, estimated by NH₃-TPD (Figure S2), varied within experimental error making it difficult to draw a conclusive conclusion.

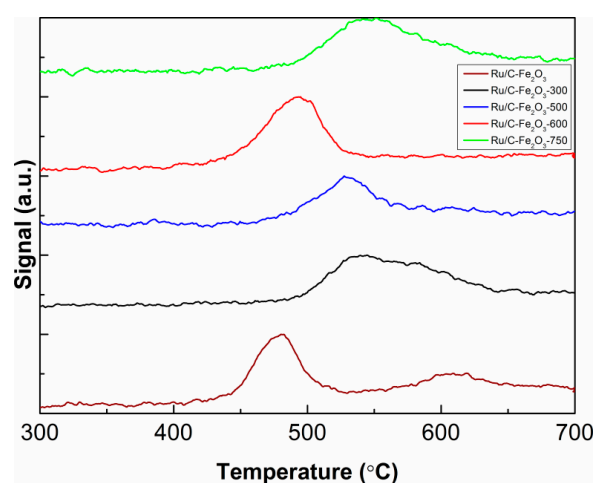


Figure 6. CO-TPD results for Ru/C-Fe₂O₃, Ru/C-Fe₂O₃-300, Ru/C-Fe₂O₃-500, Ru/C-Fe₂O₃-600, and Ru/C-Fe₂O₃-750.

3.2. Hydrotreatment Results

The prepared catalysts differed in support annealing temperatures; specifically at 300, 500, 600, and 750 °C, thus catalysts were labelled as: Ru/C-Fe₂O₃-300, Ru/C-Fe₂O₃-500, Ru/C-Fe₂O₃-600, and Ru/C-Fe₂O₃-750. The Ru/C-Fe₂O₃ label refers to a nonannealed sample. Therefore hypothesis that annealing temperature influenced catalyst activity and selectivity for the hydrotreatment of eugenol was investigated. Detected products in the liquid phase and their abbreviations: eugenol (HMAB), 2-methoxy-4-propylphenol (HMPB), 2-methoxy-4-propylcyclohexanol (HMPC), 4-propylcyclohexane-1,2-diol (HHPC), 4-propylphenol (HPB), 4-propylcyclohexanol (HPC), propylbenzene (PB), propylcyclohexane (PC), propylcyclopentane (PCP), 4-propylcyclohexanone (KPC), and isoeugenol (IHMAB). Results are summarized in Figure 7. Nonannealed catalyst showed a very low activity, as it can be seen in Figure 7a. HMAB was fully, but mostly homogeneously (noncatalytically), converted to HMPB within the heating period of the experiment according to the previous results [15] obtained without the catalyst. Further catalytic conversion of HMPB was negligible, since only approximately 2 mol% of HPB was observed in the final product, while the mole fraction of other components (HMPC, HHPC, KPC, HPC, and PC) was less than 1 mol% each. On the other hand, support annealed at the temperature of 300 °C significantly increased the final catalyst's activity and selectivity (Figure 7b). Hydrotreatment of HMAB over Ru/C-Fe₂O₃-300 after 3 h resulted in approximately 80 mol% of HPC, 9 mol% of PC, 5 mol% of HMPC, 2 mol% of PCP and KPC, and 1 mol% of PB or HPB. With further annealing temperature increase to 500 °C, catalytic activity was even higher, resulting in enhanced deoxygenation reactions and a higher yield of completely deoxygenated and hydrogenated product PC. 66 mol% of HPC, 30 mol% of PC, 2.5 mol% of PCP, and a remaining 1.5 mol% of others were detected in the final product at 275 °C (Figure 7d). Higher Ru/C-Fe₂O₃-500 selectivity towards HPC was accomplished by lowering reaction temperature to 225 °C (Figure 7c) as a result of the less promoted dehydroxylation reaction. The latter was also noticed based on a notable amount of HHPC in the system (approx. 10 mol%) during a wide reaction time interval. A fraction of this dihydroxyl intermediate was always lower than 4 mol% in all other runs. Deoxygenation has been reported as a high activation energy reaction; also confirmed in the present study (see Section 4.3), thus being unfavourable at lower temperatures resulting in low conversion of HPC at 225 °C and therefore low high final yield. The reaction mixture was cooled after 216 min and again heated up to 225 °C, with the aim to test the ability of correct model response and test eventual catalyst deactivation during the cooling-down and reheating back to reaction temperature. The catalyst treated at 600 °C has exhibited a significantly enhanced degree of deoxygenation since 80 mol% of PC was detected in the final product, 15 mol% of PCP, and the remaining 5 mol% belonged to others (mostly HPC) (Figure 7e). However, a notable amount of PCP takes side of disadvantage since ring contraction leads to unwanted carbon losses. When the catalyst's support was treated at 750 °C (Figure 7f), catalytic activity, as well as selectivity, was significantly reduced. Approximately 8.5 mol% of HMPB was still presented in the final product which was fully consumed within the first 100 min of the reaction by other prepared catalysts or Ru/C (5 wt% Ru, Sigma Aldrich, St. Louis, MO, USA, reference number 206180). Besides 8.5 mol% of HMPB, hydrotreatment of HMAB over Ru/C-Fe₂O₃-750 resulted in approximately 22 mol% of HMPC, 14 mol% of HPB, 47 mol% of HPC, 6 mol% of PC, and 2.5 mol% of others. A work by Whiffen and Smith also showed that the catalyst annealing temperature affected the product distribution [21] of 4-methylphenol HDO. Namely, the Ni₂P catalyst annealed at 550 °C and displayed the lowest selectivity towards deoxygenated products, while when annealed at 700 °C displayed the highest. The same group, one year before, published a study again showing an influence of annealing temperature on the product distribution of 4-methylphenol HDO [22] over the MoP-CA (CA-citric acid) catalyst. The MoP-CA has been annealed in a range of temperatures from 500 to 700 °C. The highest conversion was achieved on the catalyst treated at 550 °C (71%), obtaining the lowest yield of toluene. A slightly lower conversion of 4-methylphenol of 58%, but the highest selectivity towards toluene, was accomplished for the catalyst annealed at 500 °C.

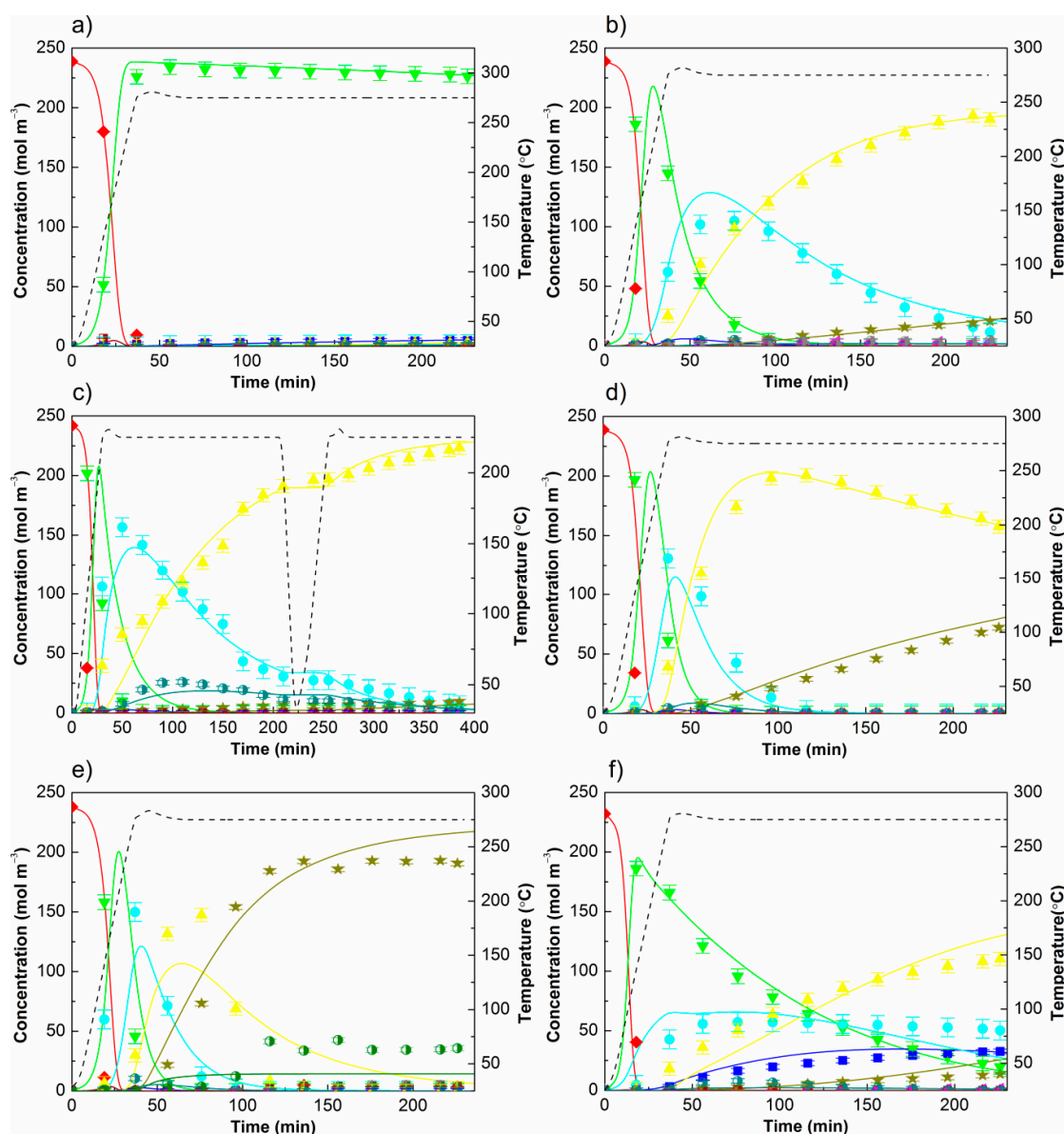


Figure 7. Experimental and model results for (a) Ru/C-Fe₂O₃, (b) Ru/C-Fe₂O₃-300, and (c) Ru/C-Fe₂O₃-500 at 225 °C, (d) Ru/C-Fe₂O₃-500 at 275 °C, (e) Ru/C-Fe₂O₃-600 and (f) Ru/C-Fe₂O₃-750. Meaning of symbols is as follows: \blacklozenge HMAB, \blacktriangledown HMPB, \blacksquare HPB, \bullet HMPC, \blacktriangleleft PB, \blacktriangle HPC, \star PC, \blacksquare IHMAB, \bullet PCP, \bullet HHPC, —temperature.

The reaction network proposed in the previous work [15] for HDO of HMAB over Ru/C has been shown to be valid for magnetic Ru catalysts according to the product evolution and distribution over the reaction time (Figure 8). Several studies proposed reaction mechanisms of lignin model compounds (phenol, m-cresol) HDO over oxophilic metals (e.g., Fe-based catalysts) to describe the observed product distribution [23,24] ruling out direct Csp₂-O bond scission. Namely, it has been reported that (substituted) phenols might be in an equilibrium with an unstable ketone intermediate (3,5-cyclohexadienol) which can be hydrogenated over an oxophilic catalyst into unsaturated cycloalcohol (3,5-cyclohexadienol). The latter can be readily dehydrated (driven by aromatic stabilization) to (substituted) benzene. However, we have not observed a significant amount of deoxygenated aromatics in contrast to reports on Fe-based catalysts [24–28]. Further comparing our results to those obtained over Ru/C (5 wt% Ru, Sigma Aldrich, St. Louis, MO, USA, reference number

206180) tested in the previous study (Figure S3) [15], one may say that our catalysts performed similar to Ru/C.

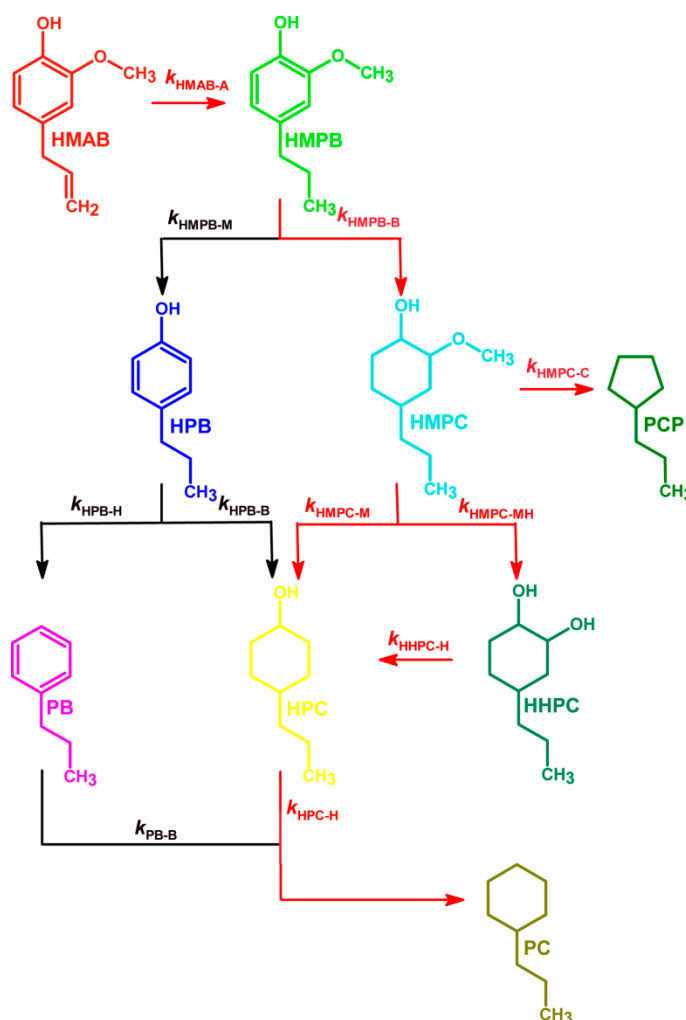


Figure 8. Eugenol reaction network over tested catalysts.

In general, an increase in annealing temperature up to 600 °C resulted in increasing HDO activity. Although further increase in the annealing temperature to 750 °C has not provided any improvement in the catalyst activity or selectivity, ring hydrogenation was of lower rate relative to other catalysts causing HPB detection of 14 mol% in the final product. Considering significant deviation from the results with Fe-based catalysts, one may say that Ru is a dominant active phase in our case where ring hydrogenation primarily took place as more favourable due to the planar adsorption of HMAB and HMPB on the Ru surface via ring [29–32]. Enhanced deoxygenation activity of catalysts annealed at higher temperature can be correlated to the dispersion and structure of Ru nanoparticles. Namely, an increase in the number of Ru nanoparticles (caused by greater reduction of Ru³⁺) and their larger dispersity (according to the XRD and TEM results) is most likely responsible for the increased HDO activity of catalysts annealed at higher temperatures. Nonannealed catalyst possesses a small amount of Ru nanoparticles that are poorly dispersed on the support surface being almost inactive. The number of Ru nanoparticles increased when the catalyst was annealed at 300 °C showing significantly higher activity compared to nonannealed. Particles were mostly clustered due to the low surface area available for impregnation causing lower activity of this catalyst accompanied by their lower amount compared to those annealed at 500 and 600 °C. When the support was annealed at 500 °C, the number of Ru nanoparticles increased further, as well as the surface area and thus dispersity. Ru reduction

proceeded even further when the support was annealed at 600 °C resulting in a larger number of Ru nanoparticles with even better dispersity on the support surface (due to even higher surface area), resulting in excellent HDO activity of this catalyst. Two types of particle shape were observed as possibly contributing to such catalytic behaviour, given that different plane might be exposed. A further increase of annealing temperature caused significant structural changes of Ru/C-Fe₂O₃-750 and, therefore, quite different activity. Considering CO TPD peak's position, it seems that the strength of active sites is mostly moderate for all catalysts, indicating no clear connection between their strength and observed activity. However, the shape could be linked to activity since the most active catalysts (annealed at 500 and 600 °C) showed sharp, strong, and narrow peak indicating the dominant existence of one active site type, which might be appropriate for both hydrogenation and deoxygenation. Fe's contribution to enhanced HDO activity is not expected or could be described as minor, as the Fe-phase in our catalysts represents a core coated by a carbon layer. Detailed TEM investigation of the support materials (prior deposition of Ru) showed that a small amount of Fe-containing nanoparticles might not be completely coated by a carbon layer when support was annealed at 600, and particularly, at 750 °C. Ru nanoparticles could be also deposited on these surfaces thus making intimate contact with Fe which can potentially cause a significant detection of HPB over Ru/C-Fe₂O₃-750. Yet this cannot be certainly said as a very thin carbon layer can be still present over the Fe core but not visible on TEM images.

Results over Ru/C are shown in supplementary information as Figure S3 (detailed results are available in the previous study) [15]. In both cases, magnetic and commercial Ru/C, Ru phase is responsible (or at least mainly) for the observed catalytic activity and is most likely making the difference between them via, for example, the degree of dispersity or the type of Ru active sites exposed. Additionally, the potential impact of Fe might not be ruled out according to the TEM results and estimated acidity of the catalysts. Namely, somewhat higher acidity has been estimated for our catalysts relative to the Ru/C, which might be expected for Fe-containing catalyst being usually correlated to the greater HDO activity [33–35]. Nevertheless, if there is a Fe contribution, it is probably rather low, as pointed out above.

3.3. Modelling Results

Adsorption–desorption equilibrium constants for hydrogen and organic components are estimated to be 3.17×10^{-2} and $3.15 \times 10^{-3} \text{ m}^3 \text{ mol}^{-1}$, respectively. Rate constants of observed reactions and activation energies accompanied are summarized in Tables 2 and 3. It might be worth highlighting that estimated reaction rate constants are already normalized on the concentration of active sites obtained from CO-TPD results being thus a direct indication of catalyst activity. Considering the provided model results, it can be noted that the catalyst's ability to hydrogenate a benzene ring increases with annealing temperature from 0 to 600 °C by two orders of magnitude between Ru/C-Fe₂O₃ and Ru/C-Fe₂O₃-300, 2.5-fold between being annealed at 300 and 500 °C, and 1.3-fold between being annealed at 500 and 600 °C, decreasing thereafter, as the catalyst annealed at 750 °C exhibited lower hydrogenation activity compared to other active catalysts, i.e. being between nonactive and annealed at 300 °C. Similarly, the increase of annealing temperature up to 600 °C facilitated deoxygenation of unsaturated and saturated intermediates (Ar–aromatics, Al–alkyl):

$$\text{Ar-OCH}_3: k_{\text{HMPB}}^{\text{cat}}(\text{Ru/C-Fe}_2\text{O}_3) \times 21 \approx k_{\text{HMPB-M}}^{\text{cat}}(\text{Ru/C-Fe}_2\text{O}_3\text{-300}) \times 1.2 \approx k_{\text{HMPB-M}}^{\text{cat}}(\text{Ru/C-Fe}_2\text{O}_3\text{-500}) \times 1.1 \approx k_{\text{HMPB-M}}^{\text{cat}}(\text{Ru/C-Fe}_2\text{O}_3\text{-600});$$

$$\text{Ar-OH}: k_{\text{HPB-H}}^{\text{cat}}(\text{Ru/C-Fe}_2\text{O}_3) \times 21 \approx k_{\text{HPB-H}}^{\text{cat}}(\text{Ru/C-Fe}_2\text{O}_3\text{-300}) \times 1.8 \approx k_{\text{HPB-H}}^{\text{cat}}(\text{Ru/C-Fe}_2\text{O}_3\text{-500}) \times 0.6 \approx k_{\text{HPB-H}}^{\text{cat}}(\text{Ru/C-Fe}_2\text{O}_3\text{-600});$$

$$\text{Al-OCH}_3: k_{\text{HMPC-M}}^{\text{cat}}(\text{Ru/C-Fe}_2\text{O}_3) \times 19 \approx k_{\text{HMPC-M}}^{\text{cat}}(\text{Ru/C-Fe}_2\text{O}_3\text{-300}) \times 3.5 \approx k_{\text{HMPC-M}}^{\text{cat}}(\text{Ru/C-Fe}_2\text{O}_3\text{-500}) \times 1.1 \approx k_{\text{HMPC-M}}^{\text{cat}}(\text{Ru/C-Fe}_2\text{O}_3\text{-600});$$

$$\text{Al-OH}: k_{\text{HPC-H}}^{\text{cat}}(\text{Ru/C-Fe}_2\text{O}_3) \times 3.2 \approx k_{\text{HPC-H}}^{\text{cat}}(\text{Ru/C-Fe}_2\text{O}_3\text{-300}) \times 2.8 \approx k_{\text{HPC-H}}^{\text{cat}}(\text{Ru/C-Fe}_2\text{O}_3\text{-500}) \times 11 \approx k_{\text{HPC-H}}^{\text{cat}}(\text{Ru/C-Fe}_2\text{O}_3\text{-600}).$$

Table 2. Heterogeneous reaction rate constants at 275 °C.

Reaction Rate Constant, $\text{m}^3 \text{mol}^{-1} \text{min}^{-1}$	Ru/C-Fe ₂ O ₃	Ru/C-Fe ₂ O ₃ -300	Ru/C-Fe ₂ O ₃ -500	Ru/C-Fe ₂ O ₃ -600	Ru/C-Fe ₂ O ₃ -750
$k_{\text{HMAB-A}}^*$	5.9×10^5	1.3×10^7	1.4×10^7	1.3×10^7	1.3×10^7
$k_{\text{HMPB-B}}^*$	1.1×10^2	7.2×10^4	1.8×10^5	2.3×10^5	1.5×10^4
$k_{\text{HMPB-M}}^*$	2.9×10^2	6.3×10^3	7.7×10^3	8.2×10^3	3.2×10^3
$k_{\text{HMPC-M}}^*$	1.2×10^3	2.3×10^4	8.1×10^4	9.0×10^4	9.3×10^3
$k_{\text{HPB-B}}^*$	1.9×10^2	1.1×10^5	1.8×10^5	2.3×10^5	2.8×10^2
$k_{\text{HPB-H}}^*$	1.5×10^1	3.1×10^2	5.7×10^2	3.3×10^2	1.1×10^2
$k_{\text{HPC-H}}^*$	4.7×10^2	1.5×10^3	4.2×10^3	4.6×10^4	2.7×10^3
$k_{\text{PB-B}}^*$	5.3×10^2	1.1×10^5	1.9×10^5	2.9×10^5	1.6×10^5
$k_{\text{HMPC-MH}}^*$	n.a.	4.3×10^2	1.5×10^4	1.1×10^4	1.2×10^4
$k_{\text{HHPC-H}}^*$	n.a.	1.1×10^4	1.3×10^5	1.8×10^5	1.4×10^5
$k_{\text{HMPC-C}}^*$	n.a.	7.3×10^1	9.8×10^1	5.9×10^3	n.a.

Generally, deoxygenation of saturated compounds was more favoured compared to the unsaturated shown also by Goncalves and coworkers [36]. Further, hydrogenation is more favoured than deoxygenation over all tested catalysts being in an agreement with other kinetic studies [37,38]. Similar to the results of Massoth et al. [38] and Shafaghat and coworkers [39], we have also observed faster hydrogenation of less substituted benzene. In fact, Massoth et al. reported a hindered hydrogenation of methyl-substituted phenols if the number of methyl groups on the benzene ring was increasing. By investigating the hydrogenation of phenol, cresol, and guaiacol over Pd/C and zeolite solid acids, Shafaghat et al. observed a beneficial effect of methyl and methoxy groups in cresol and guaiacol on direct HDO mechanism at the expense of hydrogenation. Removal of oxygen-containing groups takes place to a larger extent via C–OCH₃ bond scission then by C–OH cleavage regardless of whether it appears on saturated or unsaturated components. Such behaviour has been also observed by performing DFT calculations of guaiacol HDO over a Ru (0001) plane [30,40].

HMAB transformation into HMPB is a fast reaction over all catalysts tested. The low hydrogenation constant of HMPB for a nonannealed catalyst clearly indicates the low activity of the catalyst. Almost negligible conversion of the first intermediate slows down or disables the downstream reactions. Other tested catalysts have shown good performance in catalysing the ring hydrogenation reaction. A significant amount of HPC in the system with Ru/C-Fe₂O₃-300 was a direct consequence of 15-fold intensive formation than disappearance. This ratio was even larger in the case of Ru/C-Fe₂O₃-500 (19-fold) resulting in a sharper increase of HPC concentration which started decreasing after 100 min due to no precursor being formed and a significantly high (higher than for Ru/C-Fe₂O₃-300) rate constant of the disappearance reaction producing a notable amount of oxygen-free component PC. A further increase in the catalyst annealing temperature up to 600 °C significantly improved catalyst activity in the dehydroxylation of saturated intermediates resulting in a quantitative production of PC already at 125 min of the reaction. Only deoxygenation of unsaturated HPB and formation of HHPC were of lower rate for Ru/C-Fe₂O₃-600 relative to the Ru/C-Fe₂O₃-500, all other reaction rates were the highest estimated in this group of catalysts. Catalyst annealed at 750 °C expressed the lowest hydrogenation activity among all other tested (active). Notable lower activity of Ru/C-Fe₂O₃-750 to hydrogenate HPB (over two orders of magnitude lower compared to other active catalysts) accompanied by moderate activity to remove the OCH₃ group from HMPB which caused an appreciable detection of HPB in the system. The ratio between HMPB hydrogenation and demethoxylation clearly indicates the formation of PC via the hydrogenation route for all catalysts.

Hydrogenation of HMPB was a slightly more promoted reaction on Ru/C-Fe₂O₃-600, while demethoxylation of HMPC and dehydroxylation of HPC were 47 and 10 times faster reactions, respectively, compared to the Ru/C [15]. Demethoxylation of HMPC was also more promoted over Ru/C-Fe₂O₃-750 in comparison to Ru/C (almost five times). Ru/C is, however, more active considering all other reactions and the other three tested catalysts in general.

Activation energies of hydrogenation reactions are significantly lower than for deoxygenation reactions (Table 3). Besides, methoxy group removal is a less energy demanding reaction than the removal of hydroxyl groups, regardless of whether it occurs on a saturated or unsaturated species. Lu et al. [40], in their DFT study, reported an approximately 11 kJ mol^{-1} lower activation energy for guaiacol demethoxylation over the Ru catalyst, and 20 kJ mol^{-1} higher for hydroxyl group removal than estimated in this work. Similarly, 30 kJ mol^{-1} higher activation energy has been observed for m-cresol dehydroxylation (120 kJ mol^{-1}) by Tan et al. [9] compared to our estimation for HPB, while it was significantly higher (90 kJ mol^{-1}) for its hydrogenation. Higher activation energy of benzene ring hydrogenation (79 kJ mol^{-1}) has been also proposed by He et al. but over the Pd/C catalyst [41].

Table 3. Activation energies of heterogeneous reactions (kJ mol^{-1}).

$Ea_{\text{HMAB-A}}^*$	$Ea_{\text{HMPB-B}}^*$	$Ea_{\text{HMPB-M}}^*$	$Ea_{\text{HMPC-M}}^*$	$Ea_{\text{HPB-B}}^*$	$Ea_{\text{HPB-H}}^*$
37.5	31.5	79.3	61.0	28.5	90.2
$Ea_{\text{HPC-H}}^*$	$Ea_{\text{PB-B}}^*$	$Ea_{\text{HMPC-MH}}^*$	$Ea_{\text{HHPC-H}}^*$	$Ea_{\text{HMPC-C}}^*$	
128.3	33.2	42.2	77.3	130.0	

Product distribution has been affected by temperature as shown in Figure 7c,d, refer to results obtained at 225 and 275 °C by the same order. Concentration profiles of formed components up to 50 min of the reaction (basically of hydrogenated products) are similar at these two temperatures, indicating lower activation energies of ring hydrogenation reactions (confirmed by the model results) and, thus, their lower sensitivity to temperature changes. More significant transformations of HMPC into HPC and further into PC at higher temperature, on the other hand, suggests higher activation energies of deoxygenation reactions also predicted by the model. The observation that deoxygenation reactions become more highly promoted at higher temperatures has been reported in numerous studies [12,28].

Catalyst coverage by each component has been estimated for the Ru/C-Fe₂O₃-300 catalyst and is shown here as Figure 9 to illustrate the model abilities. Subplot a is related to the log scale of the time axis showing actual surface concentrations, while b represents the catalyst coverage by components at three reaction times. According to Figure 9a, the dominant surface components, which take up to 10 min of the reaction, are HMAB and the solvent (HD). Ring hydrogenation mostly takes place within this period causing relatively constant and low hydrogen surface concentration, while it increases thereafter. Hydrogen concentration in the liquid phase was calculated according to the actual pressure in the reactor. HPC has become the dominant surface component after 100 min of the reaction.

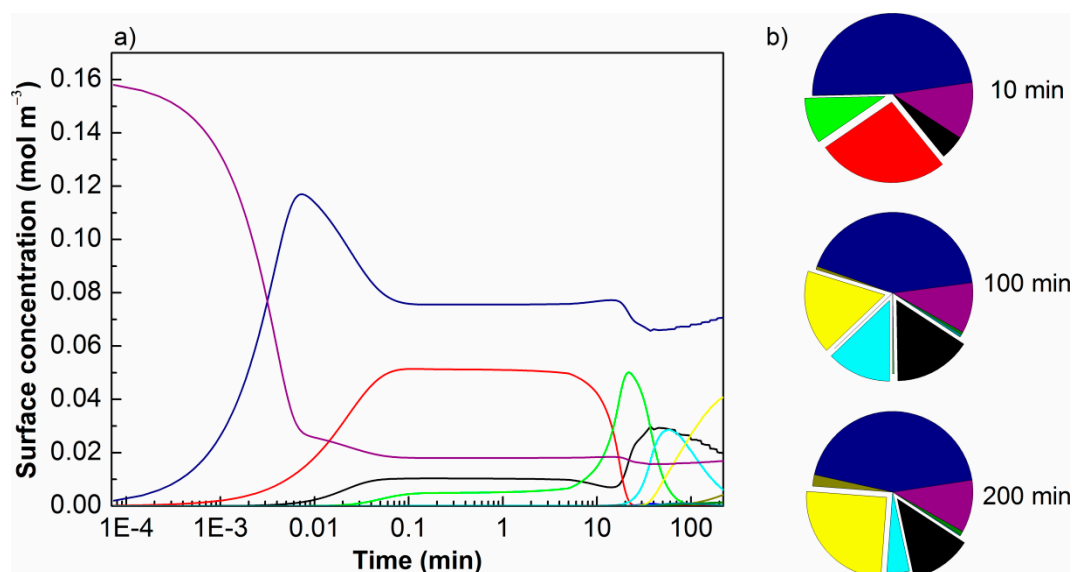


Figure 9. (a) Surface concentration on the Ru/C-Fe₂O₃-300 catalyst over the entire reaction time presented in log scale (HMAB–red, HMPB–green, HPB–blue, HMPC–cyan, PB–magenta, HPC–yellow, PC–dark yellow, IHMAB–wine, HHPC–dark cyan, hydrogen–black, solvent–navy, vacant active sites–purple); (b) Ru/C-Fe₂O₃-300 coverage by each component in % at 10, 100, and 200 min.

4. Materials and Methods

4.1. Catalyst Preparation

Catalysts were prepared in four steps. In the first step, the citric-acid coated magnetic iron oxide nanoparticles were synthesized by a simple coprecipitation of Fe²⁺ and Fe³⁺ ions, followed by citrate ion adsorption [42]. In the second step, glucose was dissolved in the colloidal suspension of citric-acid-coated magnetic iron oxide nanoparticles, transferred to the stainless steel autoclave, and treated at 180 °C for 12 h. Brown flock C-Fe₂O₃ was washed and dried at 80 °C in an oven. In the third step, the dried powders C-Fe₂O₃ were heat-treated in a tubular furnace at 300, 500, 600, and 750 °C for 12 h in Ar atmosphere. Samples are denoted as C-Fe₂O₃-X, where X stands for the heat treatment temperature. Powders were milled as 2-propanol slurries in an agate mill for 2 h. In the fourth step, the obtained suspensions were mixed with the pink solutions of Ru (III) 2,4-pentadioante in 2-propanol to reach the final concentrations of 1 g L⁻¹ of C-Fe₂O₃-X and 5 × 10⁻⁴ mol L⁻¹ of Ru³⁺. Eight-hundred millilitres of the suspension was transferred to a 1 L stainless steel Parr autoclave, purged with Ar for 30 min and, during vigorous stirring, heated to 150 °C for 10 min. Catalysts Ru/C-Fe₂O₃-X were magnetically separated from the mother liquor, washed 5 times with 2-propanol, and vacuum dried. In the case of Ru/C-Fe₂O₃-500, 600, and 750, the mother liquor was clear and colourless indicating complete reduction and deposition of Ru. More details of the Ru/C-Fe₂O₃-750 synthesis are provided in the previous work [17]. Based on mass balance, the catalysts contain 5 wt% of Ru. In the case of Ru/C-Fe₂O₃ and Ru/C-Fe₂O₃-300, the mother liquor was clear but pink indicating incomplete reduction of Ru³⁺. A list of used chemicals in this work is provided in Supplementary information.

4.2. Catalysts Characterization

X-ray powder diffraction (XRD) was used to check the phase composition (Siemens D5005 diffractometer with a monochromator in the diffracted beam, Aubrey, TX, USA). Transmission electron microscope (TEM) (Jeol JEM-2100 operated at 200 kV and equipped with JED 2300 EDXS spectrometer, Aubrey, TX, USA) was used to observe catalysts, deposited on a copper-grid-supported lacy carbon foil. Nitrogen adsorption/desorption isotherm was measured for the catalysts at liquid-nitrogen

temperature using a Nova 2000e (Quantachrome, Boynton Beach, FL, USA) nitrogen sorption analyser. Room-temperature magnetisation curves of the catalysts were measured with a Vibrating-sample magnetometer (VSM) (LakeShore 7307 VSM, Westerville, OH, USA). CO and NH₃ temperature programmed desorption (TPD) was carried out using a Micrometrics AutoChem II Chemisorption Analyser (Micrometrics, Norcross, GA, USA) instrument. The methods and characterisation procedure are described in the Supplementary information.

4.3. Hydrotreatment Test

Catalyst testing was performed in a 300 mL volume batch reactor in a completely batch regime. After 0.5 wt% of a catalyst, 5 wt% eugenol, and 84.5 wt% hexadecane was loaded, the reactor was closed. The headspace was filled with hydrogen up to 5 MPa. The reaction mixture was subsequently subjected to intensive stirring (1000 min⁻¹). The reaction was started by heating-up the reaction mixture to room temperature and then to 275 °C at a rate of 7.5 K min⁻¹. After reaching the temperature plateau, the experiment proceeded for 3 h. Liquid phase sampling took place in 20 min intervals at final temperature with one additional sample in the middle of the heat-up ramp. Gas phase samples were taken in 30 min intervals from the reached plateau onwards. Gas phase composition was determined online using gas chromatography (SRI 8610C, SRI Instruments, INC, Las Vegas, NV, USA) and Fourier transform infrared (FTIR) spectroscopy (Spectrum 100, Perkin Elmer, Waltham, MA, USA). Liquid phase samples were analysed offline using a gas chromatograph with flame ionization detector (GC-FID) (Thermo Fisher Scientific, Waltham, MA, USA) and gas chromatograph with mass spectrometer detector (GC-MS) (2010 Ultra, Shimadzu, Kyoto, Japan), equipped with (60 m × 0.25 mm × 0.25 μm, Zebron ZB-5, Phenomenex, Torrance, CA, USA) capillary column. The methodology of quantitative and qualitative (gas and liquid) sample analysis is presented in our previous publications [15,43,44].

5. Conclusions

In this work we synthesised five magnetically separable Ru nanoparticles and tested them for HDO of the representative lignin monomer model compound eugenol in a batch slurry reactor at 275 °C and 5 MPa of hydrogen. Prior to Ru impregnation, the support was treated at 0, 300, 500, 600, and 750 °C. Product distribution was significantly affected by the annealing temperature. Experimental results indicate remarkable activity of the synthesised catalysts in the HDO of eugenol which selectivity towards fully deoxygenated products could be easily tuned by carbonising the catalysts at different temperatures. Nonannealed catalyst showed no activity in eugenol HDO reactions. On the other hand, thermally treated materials expressed higher hydrogenation and saturated species deoxygenation activity with the increase of annealing temperature, reaching a maximum of 600 °C. Further increase of annealing temperature has not provided any enhancement in catalytic activity, however, a notable amount of 4-propylphenol intermediate was observed due to less selective ring hydrogenation. Catalyst treated at 600 °C showed superior catalytic performance in terms of deoxygenation of saturated intermediates in comparison to the commercially available Ru/C. Ru-phase dispersity and amount of Ru nanoparticles are most likely responsible for the observed activity, while the Fe-phase is believed to not contribute or contribute slightly. The model fitted experimental results very well, more deeply explaining the observed trends from a kinetic point of view. The future work is to be focused primarily on gaining a deeper understanding of the structure–activity relationship for various catalyst properties and by monitoring the effects on product distribution. Furthermore, it might involve an increase of complexity of the reaction mixture to investigate potential cross-interactions of lignin derived bio-oil compounds and their influence on catalyst activity and selectivity. At the very final stage, transfer from the batch to a continuous system will be considered.

Supplementary Materials: The following are available online at <http://www.mdpi.com/2073-4344/8/10/425/s1>; list of chemicals used, detailed description of the catalyst characterisation procedures, formulation of the microkinetic model, supplementary figures of catalyst separation, summarized NH₃-TPD results, and catalytic

performance of commercial Ru/C catalyst. The table with nomenclature used in this work is also provided in the supplementary materials.

Author Contributions: A.B. performed the experiments, obtained the model results, and wrote the original draft paper, M.G. coordinated the work and reviewed and edited the paper, S.G., A.K., and D.M. prepared and characterised the catalysts, S.G. also contributed to the preparation of the original draft, B.L. supervised the work.

Funding: This research was funded by the Slovenian Research Agency (research core funding Nos. P2-0089, P2-0087 and P2-0152) and the Scholarship Fund through the scholarships for study of nationals of Western Balkan states in the Republic of Slovenia (JR 177).

Acknowledgments: The authors acknowledge the financial support from the Slovenian Research Agency (research core funding Nos. P2-0089, P2-0087 and P2-0152) and Scholarship Fund through the Scholarships for study of nationals of Western Balkan states in the Republic of Slovenia (JR 177). The authors also acknowledge the use of the equipment in the Center of Excellence in Nanoscience and Nanotechnology—Nanocenter and the contribution of FPS COST Action FP1306.

Conflicts of Interest: The authors declare no conflicts of interest.

References

1. Alonso, D.M.; Wettstein, S.G.; Dumesic, J.A. Bimetallic catalysts for upgrading of biomass to fuels and chemicals. *Chem. Soc. Rev.* **2012**, *41*, 8075–8098. [[CrossRef](#)] [[PubMed](#)]
2. Breunig, M.; Gebhart, P.; Hornung, U.; Kruse, A.; Dinjus, E. Direct liquefaction of lignin and lignin rich biomasses by heterogenic catalytic hydrogenolysis. *Biomass Bioenergy* **2018**, *111*, 352–360. [[CrossRef](#)]
3. Welker, C.; Balasubramanian, V.; Petti, C.; Rai, K.; DeBolt, S.; Mendu, V. Engineering Plant Biomass Lignin Content and Composition for Biofuels and Bioproducts. *Energies* **2015**, *8*, 7654–7676. [[CrossRef](#)]
4. Zhu, H.; Luo, W.; Ciesielski, P.N.; Fang, Z.; Zhu, J.Y.; Henriksson, G.; Himmel, M.E.; Hu, L. Wood-Derived Materials for Green Electronics, Biological Devices, and Energy Applications. *Chem. Rev.* **2016**, *116*, 9305–9374. [[CrossRef](#)] [[PubMed](#)]
5. Lotfi, S.; Mollaabbasi, R.; Patience, G.S. Kinetics of softwood kraft lignin inert and oxidative thermolysis. *Biomass Bioenergy* **2018**, *109*, 239–248. [[CrossRef](#)]
6. Isikgor, F.H.; Becer, C.R. Lignocellulosic biomass: A sustainable platform for the production of biobased chemicals and polymers. *Polym. Chem.* **2015**, *6*, 4497–4559. [[CrossRef](#)]
7. Baker, D.A.; Rials, T.G. Recent advances in low-cost carbon fibre manufacture from lignin. *J. Appl. Polym. Sci.* **2013**, *130*, 713–728. [[CrossRef](#)]
8. Domenek, S.; Louaifi, A.; Guinault, A.; Baumberger, S. Potential of Lignins as Antioxidant Additive in Active Biodegradable Packaging Materials. *J. Polym. Environ.* **2013**, *21*, 692–701. [[CrossRef](#)]
9. Tan, Q.; Wang, G.; Nie, L.; Dinse, A.; Buda, C.; Shabaker, J.; Resasco, D.E. Different Product Distributions and Mechanistic Aspects of the Hydrodeoxygenation of m-Cresol over Platinum and Ruthenium Catalysts. *ACS Catal.* **2015**, *5*, 6271–6283. [[CrossRef](#)]
10. Agblevor, F.A.; Jahromi, H. Aqueous phase synthesis of hydrocarbons from reactions of guaiacol and low molecular weight oxygenates. *ChemCatChem* **2018**, in press. [[CrossRef](#)]
11. Jahromi, H.; Agblevor, F.A. Hydrotreating of guaiacol: A comparative study of Red mud-supported nickel and commercial Ni/SiO₂-Al₂O₃ catalysts. *Appl. Catal. A Gen.* **2018**, *558*, 109–121. [[CrossRef](#)]
12. Liu, B.; Zhang, Z. Catalytic Conversion of Biomass into Chemicals and Fuels over Magnetic Catalysts. *ACS Catal.* **2016**, *6*, 326–338. [[CrossRef](#)]
13. Liu, X.; Xu, L.; Xu, G.; Jia, W.; Ma, Y.; Zhang, Y. Selective Hydrodeoxygenation of Lignin-Derived Phenols to Cyclohexanols or Cyclohexanes over Magnetic CoN_x@NC Catalysts under Mild Conditions. *ACS Catal.* **2016**, *6*, 7611–7620. [[CrossRef](#)]
14. Lam, E.; Luong, J.H.T. Carbon Materials as Catalyst Supports and Catalysts in the Transformation of Biomass to Fuels and Chemicals. *ACS Catal.* **2014**, *4*, 3393–3410. [[CrossRef](#)]
15. Bjelić, A.; Grilc, M.; Likozar, B. Catalytic hydrogenation and hydrodeoxygenation of lignin-derived model compound eugenol over Ru/C: Intrinsic microkinetics and transport phenomena. *Chem. Eng. J.* **2018**, *333*, 240–259. [[CrossRef](#)]
16. Agblevor, F.A.; Jahromi, H. Aqueous-Phase Synthesis of Hydrocarbons from Furfural Reactions with Low-Molecular-Weight Biomass Oxygenates. *Energy Fuels* **2018**, *32*, 8552–8562. [[CrossRef](#)]

17. Gyergyek, S.; Kocjan, A.; Bjelić, A.; Grilc, M.; Likozar, B.; Makovec, D. Magnetically separable Ru-based nano-catalyst for the hydrogenation/hydro-deoxygenation of lignin-derived platform chemicals. *Mater. Res. Lett.* **2018**, *6*, 426–431. [[CrossRef](#)]
18. David, B.; Schneeweiss, O.; Mashlan, M.; Šantavá, E.; Morjan, I. Low-temperature magnetic properties of Fe₃C/iron oxide nanocomposite. *J. Magn. Magn. Mater.* **2007**, *316*, 422–425. [[CrossRef](#)]
19. Freel, J.; Wheeler, B.R.; Galwey, A.K. Kinetic study of the oxidation of the carbides of iron. *Trans. Faraday Soc.* **1970**, *66*, 1015–1024. [[CrossRef](#)]
20. Sing, K.S.W. Reporting Physisorption Data for Gas/Solid Systems With Special Reference to the Determination of Surface Area and Porosity. *Pure Appl. Chem.* **2009**, *57*, 603–619. [[CrossRef](#)]
21. Whiffen, V.M.L.; Smith, K.J.; Straus, S.K. The influence of citric acid on the synthesis and activity of high surface area MoP for the hydrodeoxygenation of 4-methylphenol. *Appl. Catal. A Gen.* **2012**, *419*, 111–125. [[CrossRef](#)]
22. Whiffen, V.M.L.; Smith, K.J. The Effect of Calcination Temperature on the Properties and Hydrodeoxygenation Activity of Ni₂P Catalysts Prepared Using Citric Acid. In *Novel Materials for Catalysis and Fuels Processing*; American Chemical Society: Washington, DC, USA, 2013; Volume 1132, pp. 287–300.
23. de Souza, P.M.; Rabelo-Neto, R.C.; Borges, L.E.P.; Jacobs, G.; Davis, B.H.; Sooknoi, T.; Resasco, D.E.; Noronha, F.B. Role of Keto Intermediates in the Hydrodeoxygenation of Phenol over Pd on Oxophilic Supports. *ACS Catal.* **2015**, *5*, 1318–1329. [[CrossRef](#)]
24. Nie, L.; de Souza, P.M.; Noronha, F.B.; An, W.; Sooknoi, T.; Resasco, D.E. Selective conversion of m-cresol to toluene over bimetallic Ni–Fe catalysts. *J. Mol. Catal. A Chem.* **2014**, *388–389*, 47–55. [[CrossRef](#)]
25. Hensley, A.J.R.; Hong, Y.; Zhang, R.; Zhang, H.; Sun, J.; Wang, Y.; McEwen, J.-S. Enhanced Fe₂O₃ Reducibility via Surface Modification with Pd: Characterizing the Synergy within Pd/Fe Catalysts for Hydrodeoxygenation Reactions. *ACS Catal.* **2014**, *4*, 3381–3392. [[CrossRef](#)]
26. Hong, Y.; Zhang, H.; Sun, J.; Ayman, K.M.; Hensley, A.J.R.; Gu, M.; Engelhard, M.H.; McEwen, J.-S.; Wang, Y. Synergistic Catalysis between Pd and Fe in Gas Phase Hydrodeoxygenation of m-Cresol. *ACS Catal.* **2014**, *4*, 3335–3345. [[CrossRef](#)]
27. Li, X.; Zhai, Z.; Tang, C.; Sun, L.; Zhang, Y.; Bai, W. Production of propionic acid via hydrodeoxygenation of lactic acid over Fe_xO_y catalysts. *RSC Adv.* **2016**, *6*, 62252–62262. [[CrossRef](#)]
28. Olcese, R.N.; Bettahar, M.; Petitjean, D.; Malaman, B.; Giovanella, F.; Dufour, A. Gas-phase hydrodeoxygenation of guaiacol over Fe/SiO₂ catalyst. *Appl. Catal. B Environ.* **2012**, *115–116*, 63–73. [[CrossRef](#)]
29. Garcia-Pintos, D.; Voss, J.; Jensen, A.D.; Studt, F. Hydrodeoxygenation of Phenol to Benzene and Cyclohexane on Rh(111) and Rh(211) Surfaces: Insights from Density Functional Theory. *J. Phys. Chem. C* **2016**, *120*, 18529–18537. [[CrossRef](#)]
30. Huš, M.; Bjelić, A.; Grilc, M.; Likozar, B. First-principles mechanistic study of ring hydrogenation and deoxygenation reactions of eugenol over Ru(0001) catalysts. *J. Catal.* **2018**, *358*, 8–18. [[CrossRef](#)]
31. Lee, K.; Gu, G.H.; Mullen, C.A.; Boateng, A.A.; Vlachos, D.G. Guaiacol Hydrodeoxygenation Mechanism on Pt(111): Insights from Density Functional Theory and Linear Free Energy Relations. *ChemSusChem* **2015**, *8*, 315–322. [[CrossRef](#)] [[PubMed](#)]
32. Lu, J.; Heyden, A. Theoretical investigation of the reaction mechanism of the hydrodeoxygenation of guaiacol over a Ru(0001) model surface. *J. Catal.* **2015**, *321*, 39–50. [[CrossRef](#)]
33. Cordero-Lanzac, T.; Palos, R.; Arandes, J.M.; Castaño, P.; Rodríguez-Mirasol, J.; Cordero, T.; Bilbao, J. Stability of an acid activated carbon based bifunctional catalyst for the raw bio-oil hydrodeoxygenation. *Appl. Catal. B Environ.* **2017**, *203*, 389–399. [[CrossRef](#)]
34. Gonçalves, V.O.O.; Ciotonea, C.; Arrii-Clacens, S.; Guignard, N.; Roudaut, C.; Rousseau, J.; Clacens, J.-M.; Royer, S.; Richard, F. Effect of the support on the hydrodeoxygenation of m-cresol over molybdenum oxide based catalysts. *Appl. Catal. B Environ.* **2017**, *214*, 57–66. [[CrossRef](#)]
35. Liu, X.; Jia, W.; Xu, G.; Zhang, Y.; Fu, Y. Selective Hydrodeoxygenation of Lignin-Derived Phenols to Cyclohexanols over Co-Based Catalysts. *ACS Sustain. Chem. Eng.* **2017**, *5*, 8594–8601. [[CrossRef](#)]
36. Gonçalves, V.O.O.; de Souza, P.M.; da Silva, V.T.; Noronha, F.B.; Richard, F. Kinetics of the hydrodeoxygenation of cresol isomers over Ni₂P/SiO₂: Proposals of nature of deoxygenation active sites based on an experimental study. *Appl. Catal. B Environ.* **2017**, *205*, 357–367. [[CrossRef](#)]
37. Li, C.-L.; Xu, Z.-R.; Cao, Z.-A.; Gates, B.C.; Petrakis, L. Hydrodeoxygenation of 1-naphthol catalyzed by sulfided Ni-Mo/γ-Al₂O₃: Reaction network. *AIChE J.* **1985**, *31*, 170–174. [[CrossRef](#)]

38. Massoth, F.E.; Politzer, P.; Concha, M.C.; Murray, J.S.; Jakowski, J.; Simons, J. Catalytic Hydrodeoxygenation of Methyl-Substituted Phenols: Correlations of Kinetic Parameters with Molecular Properties. *J. Phys. Chem. B* **2006**, *110*, 14283–14291. [[CrossRef](#)] [[PubMed](#)]
39. Shafaghat, H.; Sirous Rezaei, P.; Daud, W.M.A.W. Catalytic hydrogenation of phenol, cresol and guaiacol over physically mixed catalysts of Pd/C and zeolite solid acids. *RSC Adv.* **2015**, *5*, 33990–33998. [[CrossRef](#)]
40. Lu, J.; Behtash, S.; Mamun, O.; Heyden, A. Theoretical Investigation of the Reaction Mechanism of the Guaiacol Hydrogenation over a Pt(111) Catalyst. *ACS Catal.* **2015**, *5*, 2423–2435. [[CrossRef](#)]
41. He, J.; Zhao, C.; Lercher, J.A. Impact of solvent for individual steps of phenol hydrodeoxygenation with Pd/C and HZSM-5 as catalysts. *J. Catal.* **2014**, *309*, 362–375. [[CrossRef](#)]
42. Campelj, S.; Makovec, D.; Drogenik, M. Preparation and properties of water-based magnetic fluids. *J. Phys. Condens. Matter* **2008**, *20*, 204101. [[CrossRef](#)] [[PubMed](#)]
43. Grilc, M.; Likozar, B.; Levec, J. Hydrodeoxygenation and hydrocracking of solvolysed lignocellulosic biomass by oxide, reduced and sulphide form of NiMo, Ni, Mo and Pd catalysts. *Appl. Catal. B Environ.* **2014**, *150–151*, 275–287. [[CrossRef](#)]
44. Grilc, M.; Likozar, B.; Levec, J. Hydrotreatment of solvolytically liquefied lignocellulosic biomass over NiMo/Al₂O₃ catalyst: Reaction mechanism, hydrodeoxygenation kinetics and mass transfer model based on FTIR. *Biomass Bioenergy* **2014**, *63*, 300–312. [[CrossRef](#)]



© 2018 by the authors. Licensee MDPI, Basel, Switzerland. This article is an open access article distributed under the terms and conditions of the Creative Commons Attribution (CC BY) license (<http://creativecommons.org/licenses/by/4.0/>).